IJPSR Vol. 2 Issue 2 Apr - Jun (2026) 06–13

eISSN: 3139-342X

International Journal of Primary and Secondary Research (IJPSR)

International, Double-Blind, Quarterly, Peer-Reviewed, Refereed, Edited and Open Access Research Journal
Journal homepage: ijpsr.co.in

Organizational Proposal Ideologies and Incipient Concert Edges of Cation-Engineered Spinel Ferrite Nanocomposites for Gas Sensing

Anil Kumar[1], Sapna Meena[2], Harsh Bhardwaj[3], Magan Prasad[4], Mahendra Vyas[5], Raaz K Maheshwari*[6]

[1]*Assistant Professor, Department of Physics, Bangur Govt College, Didwana, Didwana-Kuchaman, Rajasthan*
[2]*Assistant Professor, Department of Chemistry, SMBM Govt Girls College, Nagaur, Rajasthan*
[3]*Assistant Professor, SRKP Girls PG College, Kishanganj, Ajmer, Rajasthan*
[4]*Professor Department of Chemistry, MSJ Govt PG College Bharatpur Rajasthan*
[5]*Assistant Professor, Department of Chemistry, Govt Engineering College, Bikaner, Rajasthan*
[6]*Freelance Investigator and Scientific Writer, Former Professor, MDSU-SBRM Govt PG College, Nagaur, Rajasthan*

* Corresponding author. E-mail address: gcacs60@gmail.com

DOI- https://doi.org/10.59436/ijpsr.v2i2.2.3139-342X

A R T I C L E I N F O

Article history:
Received 10 March 2026
Received in revised form
2 0 April 2026
Accepted 01 June 2026
Available online 16 June 2026

Keywords:

spinel ferrites; cation engineering; nanocomposites; chemiresistive gas sensors; heterojunction; oxygen vacancies

A B S T R A C T

Metal oxide chemiresistors targeting NH_3, H_2S, and NO_2 at occupational and environmental thresholds remain constrained by poor selectivity, elevated operating temperatures, and humidity interference. Spinel ferrite nanocomposites provide two design variables absent from single-composition oxide sensors: ferrite cation-site occupancy and composite junction architecture. The 2015–2024 literature on cation-engineered MFe_2O_4 composites is systematically reviewed across ferrite/metal oxide, ferrite/carbon, ferrite/conducting polymer, and bi-ferrite architectures for NH_3, NO_2, H_2S, ethanol, acetone, and toluene. $ZnO/ZnFe_2O_4$ hollow nanocages resolved acetone to 1 ppm at 290°C with a response of 25.8, outperforming both isolated phases under identical conditions. Ni substitution produced Fe/Ni-ratio-dependent barrier sensitivity, and Co substitution restricted grain growth at elevated temperatures. Cu substitution altered composite morphology and carrier transport through partner-phase-dependent mechanisms. Ferrite/carbon composites achieved 0.02 ppm acetone at room temperature but showed unstable long-term performance. Ferrite/polymer composites operated at room temperature but degraded above 150°C. Bi-ferrite heterojunctions carry no indexed chemiresistive sensing data. No study in the reviewed period connects verified A/B-site cation occupancy to composite junction behaviour and sensing outcome within a single controlled experiment. Zn/Ni co-doped ferrite composites with Mössbauer-confirmed occupancy, systematic ratio variation, and humidity-controlled sensing represent the primary unresolved experimental target in cation-engineered composite sensing.

Introduction

NH_3 above 50 ppm (OSHA PEL), H_2S above 100 ppm (IDLH), and NO_2 exceeding 25 μg/m³ (WHO 24-hour guideline) mark the exposure thresholds at which chemiresistive detection is required across agriculture, mining, refinery operations, automotive emission testing, and clinical breath diagnostics.[1-3] Metal oxide chemiresistors, the dominant deployed platform for these applications, do not meet this requirement reliably. They require operating temperatures between 200 and 500°C, trade selectivity for sensitivity, and shift baseline resistance with humidity in ways that corrupt measurement accuracy in real ambient and exhaled-breath conditions.[1,2,4] ZnO and SnO_2 account for the largest body of chemiresistive sensing literature, supported by reproducible synthesis and response data across a range of gas targets.[5] Forming ZnO/SnO_2, ZnO/In_2O_3, and CeO_2/ZnO heterostructures creates interfacial charge-depletion zones that reduce optimal sensing temperatures, but selectivity improvements from these configurations are analyte-specific and do not transfer to new targets without re-optimisation.[6-8,11] The limitation is structural, not synthetic. In a binary oxide composite, electronic structure and interface geometry are coupled: adjusting the stoichiometry of one phase to modify conductivity simultaneously alters its contact geometry with the second phase, and the two cannot be optimised independently.[9] Spinel ferrite nanocomposites separate these two parameters. The cation arrangement and A/B-site occupancy within the ferrite lattice set the electronic structure of the sensing phase, while the composite partner independently establishes heterojunction type and band alignment, and neither choice constrains the other.[9,10]

Cation engineering here denotes substitution at 8a (tetrahedral) or 16d (octahedral) Wyckoff positions in MFe_2O_4, with verified consequences for carrier concentration, oxygen vacancy density, and adsorption-site chemistry.[12-14] The importance of this precision is measurable: cation inversion in $ZnFe_2O_4$ shifted NOx adsorption energy on the oxygen-covered surface from −0.1 eV to −0.6 eV, enabling ppb-level room-temperature NO detection through a mechanism that grain-size control alone cannot replicate.[12,15] These site-level changes propagate to the ferrite-second phase interface by altering band alignment and charge transfer kinetics, reconfiguring the depletion or accumulation barrier that determines sensor response.[1,8,9] That propagation is the structural basis for this review's approach. Four composite configurations are covered, bound to 2015–2026 literature: ferrite/metal oxide, ferrite/carbon nanostructure, ferrite/conducting polymer, and bi-ferrite systems.[9,14,16] Ferrite/metal oxide composites are examined because oxide-oxide junctions, whether n-n, p-n, or p-p type depending on the ferrite carrier type, modify depletion layer width and reduce optimal sensing temperature in ways directly relevant to

NH_3, NO_2, and H_2S detection.[8,20] Carbon nanostructure composites enter for their effect on interfacial charge carrier mobility and surface oxygen adsorption at the ferrite grain.[21] Ferrite/conducting polymer composites are included because polymer-oxide p-n junctions enable room-temperature chemiresistive response without external heating, a property unavailable in purely inorganic systems, though humidity-dependent baseline drift in these architectures remains inadequately characterised.[22,23] Target analytes are NH_3, NO_2, H_2S, ethanol, acetone, and toluene.[1,17-19] Studies focused on magnetic properties, photocatalytic systems, microwave absorption, and biomedical composites are excluded, as are single-phase ferrites without a composite sensing partner.[13,14,24]

2.0 Spinel Ferrites: Crystal Structure, Sensing Fundamentals, and Composite Classification

2.1 Crystal Structure and Cation Site Configuration- MFe_2O_4 spinel ferrites crystallise in space group $Fd\bar{3}m$ on a cubic close-packed oxygen sublattice that defines two distinct cation environments: tetrahedral A sites (8a Wyckoff) and octahedral B sites (16d Wyckoff).[9,25,26] The unit cell contains 8 A and 16 B positions.[26,28] These counts arise from one-eighth of all tetrahedral voids and one-half of all octahedral voids being occupied, and lattice parameters across representative MFe_2O_4 compositions span 8.3–8.5 Å, with values near 8.34 Å and 8.37–8.39 Å documented for distinct stoichiometries.[26,27,28]

Whether M^{2+} and Fe^{3+} distribute as normal, inverse, or mixed spinels depends on the site-energy preference of the divalent cation.[25,26,28] $ZnFe_2O_4$ is the canonical normal spinel, with Zn^{2+} at A sites and Fe^{3+} at B sites.[10,26,28] $NiFe_2O_4$ and $CoFe_2O_4$ are inverse spinels in which Fe^{3+} occupies A sites while M^{2+} and Fe^{3+} share B sites, and compositions between the two extremes are described by an inversion parameter λ recording the fraction of M^{2+} displaced to octahedral coordination.[25,26,28] Site occupancy governs which cations are exposed at grain surfaces and composite interfaces, directly determining the adsorption and charge-transfer pathways available for gas sensing.[25,29]

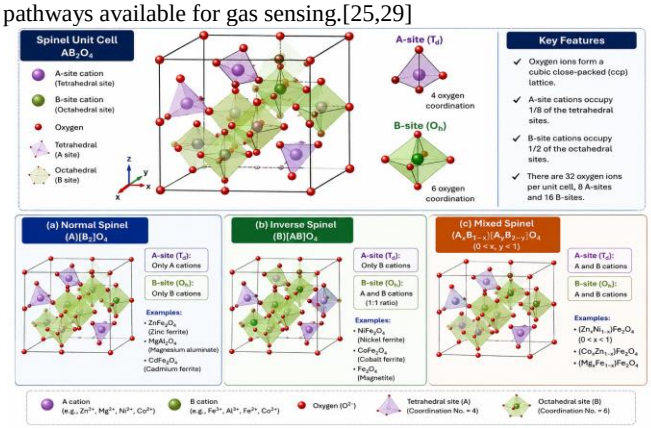

Figure 1: Spinel unit cell with A and B sites labeled; normal vs inverse vs mixed configurations with named examples. Original schematic only, not redrawn from a single source.

2.2 Electrical Conduction and Gas Sensing Mechanism-Small polaron hopping governs electrical transport in polycrystalline spinel ferrites.[30-32] Electron transfer between Fe^{2+} and Fe^{3+} on octahedral B sites provides the primary conduction pathway, with hopping site density and accessibility modulated by mixed-valence cation occupancy and site distribution.[29,32] Grain-boundary resistance, not bulk grain conductivity, dominates the net chemiresistive output in most polycrystalline ferrite sensors.[27,30,31] Carrier type divides the ferrite family: $NiFe_2O_4$ and $CoFe_2O_4$ are p-type, while $ZnFe_2O_4$ is n-type, and this distinction determines whether coupling with a composite second phase generates a p-n, n-n, or p-p junction at the shared interface.[9,20,28,33]

Chemiresistive response depends on sequential oxygen ionosorption at the oxide surface.[9,33,34] Below approximately 150°C, adsorbed O_2 captures surface electrons to form O_2^-; between 150 and 300°C, activation proceeds as $O_2^- + e^- \rightarrow 2O^-$, raising surface acceptor density.[33,35] Oxygen vacancies replenish these acceptor sites.[33,35,36] Response magnitude in n-type ferrites decreases under reducing gas exposure as electrons return to the conduction band, whereas p-type ferrites respond in the opposite direction through hole accumulation modulation; Ra/Rg and Rg/Ra conventions apply to reducing and oxidising gases, respectively.[9,33,34] CuS formation on Cu-containing sensing phases during H_2S exposure represents a chemical transformation mechanism that supplements ionosorption and is examined in Section 4.[36]

2.3 Composite Classification-Four composite architectures organise the gas-sensor literature covered in this review.[9] Type I (Ferrite/Metal Oxide) pairs a ferrite with ZnO, SnO_2, TiO_2, In_2O_3, or WO_3, and the oxide-oxide contact generates a heterojunction that modifies depletion layer width and barrier height depending on the carrier types of both components.[9,20] Type II (Ferrite/Carbon Nanostructure) uses rGO, graphene, MXenes, or CNTs with Schottky-like or ohmic contact character set by work function alignment between the ferrite and the carbon component.[21] Type III couples ferrites with PANI or PPy to enable room-temperature response, with the practical ceiling imposed by polymer thermal degradation above approximately 150°C.[10] Type IV (Bi-Ferrite) pairs two spinel ferrites of complementary carrier type to form an internal p-n junction, and their shared crystal structure reduces interfacial structural discontinuity relative to ferrite-oxide pairings.[9,33] This taxonomy structures Section 4.[9]

3.0 Synthesis of Spinel Ferrite Nanocomposites-

The synthesis route determines ferrite particle size, crystallinity, and interfacial contact quality with the composite second phase, three structural variables that directly condition sensing performance.

3.1 Co-precipitation-Aqueous metal salt solutions are brought to controlled pH by dropwise addition of NaOH or NH_4OH under mechanical agitation and mild heating at 80–100°C, precipitating metal hydroxides that convert to the ferrite phase on continued thermal treatment.[37] Particle sizes in co-precipitated ferrites typically fall within 10–30 nm, with distributions narrowing when surfactants or controlled reagent addition rates are employed.[37,39] The second phase is introduced into the precipitation medium before ferrite nucleation, so growing ferrite nuclei form on or around a pre-existing substrate, a geometry well-suited to Type II composites built on carbonaceous supports such as rGO.[37] Post-synthesis annealing improves crystallinity but drives grain growth and reduces effective contact area at the ferrite-second phase boundary, which is the primary structural cost of this route.[37] $CoFe_2O_4$/ZnS composites produced this way demonstrate that both phases integrate during precipitation without separate high-temperature processing steps.[37]

3.2 Sol-Gel Auto-Combustion-Stoichiometric metal nitrates and a chelating organic fuel (citric acid, gelatin, or polyacrylic acid) dissolved in aqueous solution form a viscous gel that undergoes self-sustaining ignition, yielding phase-pure ferrite in a single thermal step.[37] Combustion intensity, cation homogeneity, and ferrite crystallinity all respond to the fuel-to-nitrate ratio, and product particle sizes before further annealing fall in the 20–50 nm range.[37] Precursors for the composite second phase are dissolved or dispersed into the sol before gelation, producing intimate ferrite-oxide contact after combustion and making this route well-suited to Type I composites.[37] Carbon-based second phases (rGO, CNTs) oxidise during the self-sustaining thermal reaction, rendering this route incompatible with Type II composites.[37,38] $CoFe_2O_4$-SiO_2 composites produced by incorporating silica precursors into the gel before ignition illustrate the route's capacity for generating interpenetrating oxide-oxide networks.[37]

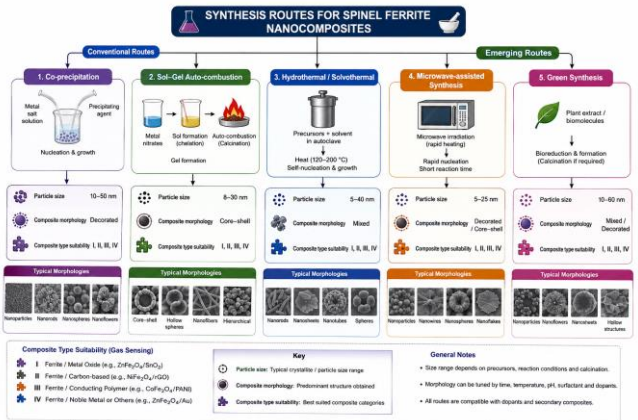

Figure 2: Schematic representation of conventional and emerging synthesis routes for spinel ferrite nanocomposites, highlighting particle

size ranges, resulting composite morphologies, and suitability for different gas-sensing composite architectures.

3.3 Hydrothermal, Microwave, and Green Synthesis- Sealed autoclave conditions at 120–220°C give hydrothermal and solvothermal processing simultaneous control over ferrite nucleation rate, crystal morphology, and second-phase integration geometry, with less agglomeration than low-temperature wet routes.[37] Second-phase incorporation follows two distinct strategies: growing ferrite directly on a pre-formed substrate (rGO sheet or oxide support) yields decorated morphologies with high interfacial contact area, while co-processing both phases within the same autoclave step produces core-shell or bi-phase architectures, with both strategies documented across all four composite types.[37] Reproducibility depends on autoclave pressure, solvent identity, surfactant concentration, and temperature uniformity, complicating transfer between laboratory and production scale.[37]

Reaction times shrink from hours to minutes under microwave dielectric heating, with resulting crystallinity matching hydrothermal benchmarks in laboratory-scale demonstrations, but composite batch reproducibility has not been validated at scale.[37] Plant extracts replace organic solvents in green synthesis, functioning simultaneously as reducing, capping, and stabilising agents and enabling Type I composite formation at lower temperatures, but ferrite crystallinity and phase purity in these products are more variable than in combustion or hydrothermal routes, and composite-specific sensing data for both emerging methods remain too sparse to benchmark them against established approaches.[37,38]

Table 1. Synthesis routes for spinel ferrite nanocomposites: particle size, composite morphology, compatible types, and primary limitation.

Synthesis Method	Particle Size (nm)	Composite Morphology	Compatible Types	Primary Limitation
Co-precipitation	10–30	Decorated (ferrite on pre-formed substrate)	Type II	Annealing drives grain growth and reduces interfacial contact area
Sol-gel auto-combustion	20–50	Intimate mixed-phase	Type I	Combustion temperatures oxidise carbon-based second phases
Hydrothermal/solvothermal	50–200	Decorated, core-shell, bi-phase	Types I–IV	Reproducibility sensitive to pressure, solvent, and temperature uniformity
Microwave-assisted	20–100	Decorated, mixed-phase	Types I–II	Batch reproducibility and scalability not validated
Green synthesis	Variable	Mixed-phase	Type I	Crystallinity and phase purity inferior to chemical routes

4.0 Cation Engineering and Composite Architecture in Ferrite Gas Sensors

4.1 Cation Site Effects on Ferrite Electronic Structure-Five parameters structure the analysis of cation substitution in ferrite nanocomposites: site occupancy at A or B positions, lattice parameter shift, oxygen-vacancy generation, conductivity change, and composite sensing outcome.[9,14] XPS and impedance spectroscopy can resolve cation oxidation states, partial occupancies, and inversion profiles directly in the ferrite phase, connecting compositional decisions to the surface electronic structure that contacts the second phase.[14,41] In a composite, those ferrite-side parameters carry into heterojunction behavior because ferrite carrier type, vacancy chemistry, and surface reactivity collectively set the interfacial barrier height, depletion width, and charge-transfer rate to the partner material.[9,20,45] Two constraints apply specifically to composites and carry through each dopant subsection: configuration can invert ferrite carrier type independently of composition, shown by n-type and p-type responses from identically composed $Mg_{0.5}Zn_{0.5}Fe_2O_4$ nanotubes under different geometric embedding conditions, and carrier type for specific ferrite phases varies across the literature with synthesis and defect state rather than being fixed by stoichiometry alone.[9,43,20]

Zn-substituted ferrites. $ZnFe_2O_4$ is among the most studied ferrite phases for chemiresistive sensing, with element doping and heterostructure formation identified as its principal performance routes.[9,42] Band-gap offset at the ZnO-$ZnFe_2O_4$ contact drives a temperature-dependent n-p-n conductive switch in hollow ZnO/$ZnFe_2O_4$ microspheres during VOC sensing, as carrier partitioning between the two phases shifts with temperature and reducing-gas electron injection.[9] Hollow nanocage ZnO/$ZnFe_2O_4$ architecture reached response 25.8 to 100 ppm acetone at 290 °C with a 1 ppm detection limit, exceeding both ZnO hollow nanocages and $ZnFe_2O_4$ nanospheres tested under identical conditions.[9] Adding Au decoration to produce ternary ZnO/$ZnFe_2O_4$/Au porous nanonets raised the response to 30.3 with 1 s response time and 59 s recovery, roughly three times the undecorated binary value.[9] The interface origin of this performance cascade is documented in the indexed corpus; the site-level cation mechanism within the ferrite lattice is not directly resolved.[9]

Ni-substituted ferrites. The carrier type for $NiFe_2O_4$ is not consistent across the indexed literature: one ferrite materials review assigns it n-type character while a gas-sensor heterojunction review places p-$NiFe_2O_4$ as a component in a p-p composite with NiO, pointing to synthesis conditions and defect equilibrium as the governing variables rather than composition alone.[43,20] Composite performance data are more internally consistent. Optimal Fe/Ni ratio in NiO nanosheets bearing in situ formed $NiFe_2O_4$ nanoparticles produced a response of approximately 23 to 50 ppm acetone at 280°C, attributed to barrier height reduction at the heterojunction surface under gas exposure, and NiO/Ni-ferrite composites altered analyte selectivity relative to pure Ni-ferrite, confirming that the interface modifies sensing chemistry rather than just amplifying response.[20,44] Reliable junction-class assignment for $NiFe_2O_4$-based composites requires synthesis-controlled carrier characterisation before p-n or p-p designation can be made.[43,20]

Co-substituted ferrites. Co-substituted ferrites carry stronger evidence for microstructural stability than for uniquely advantaged interfacial sensing chemistry.[48,46] A cobalt ferrite nanocomposite on an interdigitated electrode structure demonstrated ethanol sensitivity, dynamic range, and selectivity at concentrations down to 7 ppm.[48] Direct evidence for Co A/B site redistribution, lattice contraction, or non-monotonic resistivity in gas-sensing composite systems is absent from the indexed corpus.[48,46] Preserving interfacial contact area and structural integrity at elevated operating temperatures is the best-documented composite role for Co substitution, making synthesis route selection for morphology control a more productive lever than Co compositional variation at the current state of composite gas-sensing evidence.[40,46]

Cu-substituted ferrites. Cu incorporation modifies composite morphology distinctively: replacing Ni^{2+} with Cu^{2+} in $Co_{0.5}Zn_{0.25}M_{0.25}Fe_2O_4$ coupled to TiO_2 changed nanocomposite morphology relative to the Ni-substituted analog.[43] Cu-substituted $NiFe_2O_4$ in CNT composites showed higher conductivity than unsubstituted $NiFe_2O_4$/CNT equivalents, establishing that Cu opens more favourable carrier transfer pathways at the ferrite-carbon contact.[50] PANi/Cu-ferrite composites delivered higher room-temperature NH_3 response than pure Cu-ferrite films, confirming a detection pathway added by the polymer-ferrite junction that is absent in the single-phase material.[44] The Jahn-Teller-to-vacancy mechanism and CuS formation during H_2S sensing are not directly established in the supplied corpus, though the documented sensitivity of Cu-bearing ferrite composites to partner phase and architecture makes this class a high-priority target for interface-resolved studies.[43,44,50]

Rare-earth-substituted ferrites. La-doped Mg-ferrite and Ce-doped Co-ferrite are reported to improve sensitivity or lower operating temperature relative to undoped analogs, and Tb-doped Fe_2O_3 nanotubes reached a response of 53.2 to 50 ppm acetone at 170 °C, attributed in part to elevated oxygen vacancy concentration from the large aliovalent substituent.[14,44,46] Systematic data on RE site occupancy thresholds, secondary phase formation, or ferrite-second phase contact zone chemistry in RE-doped composite systems are absent from the indexed literature.[14,44,45] Direct characterisation at the ferrite-partner contact zone is the clearest experimental gap for the RE dopant class because RE segregation is predicted at exactly the location where composite sensing performance is determined but has not been measured in a gas-sensing context.[14,45]

4.2 Composite Architecture and Interfacial Design-The carrier type determined by cation engineering in Section 4.1 defines the junction character of the composite. Four architectures produce distinct interfacial barriers: Type I (ferrite/metal oxide) generates oxide-oxide heterojunctions, Type II (ferrite/carbon nanostructure)

generates Schottky or ohmic contacts, Type III (ferrite/conducting polymer) generates organic-inorganic junctions, and Type IV (bi-ferrite) generates internal junctions between complementary ferrite phases.[9,20] Response amplification in all four cases originates at the interface rather than from either component individually.[20,45] Band alignment at the contact governs whether the depletion layer widens or narrows during gas exposure, with direction set by the relative electron affinity and work function of both phases.[45,20]

Type I oxide-oxide junctions span n-n, p-n, and p-p configurations depending on the carrier types of both the ferrite component and the oxide partner selected.[20,9] Each configuration differs in depletion layer width and interfacial potential barrier height.[20] In n-n systems ($ZnFe_2O_4$/ZnO, $ZnFe_2O_4$/SnO_2), depletion extends from the lower-electron-affinity phase; p-n junctions such as $NiFe_2O_4$/ZnO project a built-in field into both phases, raising baseline resistance and amplifying response; p-p composites such as $NiFe_2O_4$/NiO replace depletion-layer physics with carrier balance between phases as the dominant modulation mechanism.[20,45] $NiFe_2O_4$/NiO nanosheets achieved approximately 23 responses to 50 ppm acetone at 280 °C through Fe/Ni-ratio-controlled barrier adjustment at the p-p junction.[20] The ZnO/$ZnFe_2O_4$ n-n case is documented in Section 4.1.[9] Band alignment from cation engineering determines which phase donates electrons during gas exposure; junction type, therefore, cannot be designed independently of the dopant choices in Section 4.1.[45,20] Type IV (bi-ferrite) composites form internal p-n junctions from two spinel ferrites of complementary carrier type, with shared crystal structure reducing lattice mismatch relative to ferrite-oxide pairings.[9] Systematic comparative data for Type IV systems in ferrite gas sensing are absent from the indexed corpus, and junction dynamics at the ferrite-ferrite contact zone remain unresolved.[9]

Type II (ferrite/carbon nanostructure) composites use rGO, graphene, MXenes, or CNTs as the second phase, with Schottky-like or ohmic contact determined by work-function alignment between the ferrite and the carbon component.[21] rGO/metal oxide composites consistently improve sensing over single-phase oxides by increasing accessible surface area and modifying interfacial charge carrier mobility.[21] Ferrite/graphene systems show improved carrier transport through the graphene network, and Cu-substituted $NiFe_2O_4$/CNT composites showed higher conductivity than unsubstituted equivalents, confirming that cation substitution in the ferrite phase propagates to charge transfer at the ferrite-carbon contact.[47,50] Type III (ferrite/conducting polymer) composites pair ferrites with PANI or PPy to establish room-temperature chemiresistive sensing through polymer-oxide junctions.[44,48] Flexible PANi-$CoFe_2O_4$ nanocomposite films demonstrated trace-level NH_3 sensing at room temperature, with the polymer-ferrite junction amplifying response beyond single-phase values.[23] Polymer thermal degradation above approximately 150 °C sets the operational ceiling for all Type III architectures.[44,48]

Morphological architecture within each composite class independently conditions sensing outcomes. One-dimensional electrospun structures deliver high surface-area-to-volume ratios and controlled pore channels that improve gas diffusion to the active ferrite-second phase contact.[46] Decorated morphologies, with ferrite nanoparticles on a second-phase substrate, maximise interfacial contact area; core-shell architectures require gas diffusion through the outer shell before reaching the junction, reducing response at equivalent composition; mixed-phase configurations occupy an intermediate position.[9,46] Ferrite-composite literature identifies morphology control and ion substitution as complementary rather than independent performance levers, and systematic mechanistic studies relating weight ratio to depletion width or vacancy accessibility are absent from the composite gas-sensing corpus.[9,49]

4.3 Interface Coupling and Research Gap- Three propositions are consistently supported across the indexed corpus regardless of composite type or dopant class.[9,14,20] Cation distribution between A and B sites is a primary electronic control variable in spinel ferrites; substitution modifies surface chemistry and electronic structure in ways that alter gas adsorption, and heterojunction construction amplifies sensing through interfacial barrier modulation.[9,14,20] The absent step connects them: no indexed study systematically links verified cation site occupancy in the ferrite phase to composite junction type, barrier height, and sensing output through a single controlled experimental design.[9,14] That link matters because composite architecture can override single-phase ferrite predictions, as the $Mg_{0.5}Zn_{0.5}Fe_2O_4$ embedding experiment demonstrates: configuration alone inverts carrier type without any compositional change.[9] The gap is sharpest for co-doping. Zn + Ni is mechanistically coherent, as Zn^{2+} redistributes Fe to B sites, increasing the hopping carrier pool, while Ni^{2+} at B sites introduces a second redox-active cation environment, and the two effects are additive in principle.[9,14] Cu + Zn carries similar logic through two independent vacancy generation mechanisms.[9,14] No composite study with confirmed co-dopant site occupancy, systematic ratio variation, and humidity-resolved sensing data exists for either combination.[9,14] Ferrite and sensor literature in adjacent fields repeatedly identifies deliberate interface characterisation and structure-property resolution as primary unmet needs.[14,51]

Four experimental targets define the near-term research priority. First, Zn/Ni co-doped ferrite composites require Mössbauer spectroscopy-confirmed site occupancy alongside heterojunction characterisation and humidity-controlled sensing measurements, since no study delivers all three elements simultaneously.[9,14] Second, Cu-substituted ferrite composites need long-term H_2S cycling data to establish whether CuS formation under composite sensing conditions is reversible.[9] Third, RE-doped composites require structural characterisation at the ferrite-second phase contact zone specifically, where RE segregation is predicted to concentrate but has not been measured in any study combining gas sensing with interface verification; high-resolution TEM or Mössbauer spectroscopy at the ferrite-partner boundary would directly address this gap.[14,45] Fourth, systematic comparison of composite types I through IV for a single cation-engineered ferrite composition does not exist and would close the largest outstanding gap in composite design knowledge.[9,14]

Table 2. Cation substitution effects on ferrite electronic structure, expected composite junction, and confirmation status in indexed composite gas sensing.

Dopant	Preferred Site	Lattice Response	Vacancy Generation	Conductivity Effect	Expected Junction	Composite Confirmed
Zn^{2+}	A (tetrahedral)	Expansion	Moderate	Fe^{3+} redistributed to B sites; lowered resistivity; n-type	n-n (ZnO, SnO_2)	Yes, ZnO/$ZnFe_2O_4$ response 25.8 documented
Ni^{2+}	B (octahedral)	Slight contraction	Moderate	Ni^{2+}/Ni^{3+} redox couple; carrier type synthesis-dependent	p-n or p-p	Yes, Fe/Ni-ratio-dependent barrier modulation confirmed
Co^{2+}	A and B (mixed)	Contraction	Moderate	Non-monotonic resistivity with substitution level	p-n or n-n	No
Cu^{2+}	B (octahedral)	Jahn-Teller distortion	High	Cu^{+}/Cu^{2+} couple; reduced hopping activation energy	Partner-phase-dependent	No, CuS mechanism unverified in composite
RE^{3+}	Grain boundary	$REFeO_3$ above $x \approx 0.10$	High at boundaries	Grain boundary pinning; interface chemistry	Varies with partner	No, contact zone uncharacterised

	above x ≈ 0.05			modified		
Zn^{2+} + Ni^{2+}	A (Zn) + B (Ni)	Additive expansion and contraction	Moderate to high	Combined n-type strengthening and dual redox couple	n-p hybrid (predicted)	No, primary unresolved experimental target

5.0 Comparative Gas Sensing Performance- Composite ferrite sensing data in the indexed corpus concentrate on acetone and VOC detection. Organising performance by composite architecture type rather than by analyte reflects actual coverage and avoids implying balanced gas-target data where none exists.

5.1 Type I: Ferrite/Metal Oxide Composites- ZnO/$ZnFe_2O_4$ hollow nanocages registered response 25.8 to 100 ppm acetone at 290°C and resolved the analyte to 1 ppm.[9] ZnO hollow nanocages and $ZnFe_2O_4$ nanospheres tested independently under identical conditions both underperformed the composite, which localises the gain at the oxide-oxide contact rather than in either phase.[9] Au-functionalised ZnO/$ZnFe_2O_4$ porous nanonets extended response to 30.3 with 1 s response time and 59 s recovery, approximately three times the undecorated binary values.[9] A second ZnO/$ZnFe_2O_4$ morphology covered 5 to 700 ppm acetone at 250°C.[53] In a p-p type I architecture, $NiFe_2O_4$-decorated NiO nanosheets at Fe/Ni-24.9 composition reached a response of approximately 23 to 50 ppm acetone at 280°C, with the performance optimum tracking the compositional ratio rather than total ferrite loading.[20,52] NH_3, NO_2, and H_2S data are absent for all Type I ferrite composites in the supplied literature.

5.2 Type II: Ferrite/Carbon Nanostructure Composites- rGO/WO_3/$ZnFe_2O_4$ reached response 26.92 to acetone with a 0.02 ppm detection limit and 51 s response time, exceeding both WO_3 and $ZnFe_2O_4$ individually under matched conditions.[9] $ZnFe_2O_4$/graphene quantum dot composites operated at room temperature and covered acetone from 5 ppm at a response of 1.2 to 1000 ppm at a response of 13.3, with response and recovery times each under 12 s; long-term stability was reported as unsatisfactory in the same study.[9] Room-temperature operation in these two Type II systems distinguishes the carbon composite architecture from Type I entries, which required 250–290°C to reach comparable response values.[9,53] NH_3, H_2S, and toluene data for ferrite/carbon composites are absent from the indexed literature.

5.3 Type III: Ferrite/Conducting Polymer Composites- PANI/Cu-ferrite films produced higher NH_3 response at room temperature than Cu-ferrite alone under matched conditions, with the polymer-ferrite junction contributing a charge transfer pathway inactive in the single-component material.[44] SnO_2/PANI, a non-ferrite reference case spans 10 ppb to 100 ppm NH_3 at room temperature, a concentration window against which no ferrite-polymer composite has yet been benchmarked.[53] Thermal degradation of the conducting polymer above approximately 150°C limits all Type III architectures, and no indexed ferrite-polymer composite study reports stability data beyond 7 days of continuous operation.[44,48]

5.4 Type IV: Bi-Ferrite Composites- Bi-ferrite Type IV composites carry no performance entries in the indexed gas sensing literature.[9] Whether a ferrite-ferrite p-n junction produces a response distinct from single-phase ferrite behaviour under gas exposure has not been tested for any analyte or operating condition.[9] A direct comparison between $NiFe_2O_4$/$ZnFe_2O_4$ and each isolated constituent would close this gap at the minimum experimental cost.[9]

Table 3. Indexed composite spinel ferrite gas sensing performance (2015–2024) organised by composite type; dashes indicate unreported values; nine entries represent the complete dataset from the supplied corpus, with NH_3, NO_2, H_2S, and toluene absent for Types I and II, and Type IV unrepresented.

Composite Type	Material	Target Gas	Temp (°C)	Response	LOD	Reference
Type I	ZnO/$ZnFe_2O_4$ hollow nanocages	Acetone	290	25.8 (100 ppm)	1 ppm	[9]
Type I	ZnO/$ZnFe_2O_4$/Au nanonets	VOC	—	30.3	—	[9]
Type I	ZnO/$ZnFe_2O_4$	Acetone	250	—	5 ppm	[53]
Type I	$NiFe_2O_4$/NiO nanosheets	Acetone	280	~23 (50 ppm)	—	[20,52]
Type II	rGO/WO_3/$ZnFe_2O_4$	Acetone	—	26.92	0.02 ppm	[9]
Type II	$ZnFe_2O_4$/graphene QD	Acetone	RT	13.3 (1000 ppm)	5 ppm	[9]
Type II	$ZnFe_2O_4$/graphene QD	Acetone	RT	1.2 (5 ppm)	—	[9]
Type III	PANI/Cu-ferrite	NH_3	RT	Above single-phase	—	[44]
Type IV	—	—	—	—	—	—

All entries represent the complete indexed composite ferrite sensing dataset from the supplied corpus. Row gaps reflect absent data. NH_3, NO_2, H_2S, ethanol, and toluene are unrepresented for Types I and II; H_2S and VOC coverage are absent for Type III; Type IV carries no entries.

6. Challenges and Future Perspectives

6.1 Selectivity- Cross-sensitivity between NH_3 and H_2S is structurally difficult to resolve in ferrite composite systems because both gases reduce surface-adsorbed oxygen species through electron donation, generating resistance changes in the same direction and at comparable magnitude in n-type architectures.[1,9] Selectivity stands as a primary barrier to chemiresistive sensor commercialisation across metal oxide platforms, and ferrite composites have not addressed this at the junction level.[1] Temperature-selective windows, in which different analytes produce maximum response at different operating temperatures, have been described as a partial strategy in single-phase oxide systems but remain unvalidated for any ferrite composite architecture in the indexed corpus.[1,53] No indexed study demonstrates analyte discrimination in a ferrite composite through deliberate heterojunction design, meaning through controlled variation of junction type or barrier height rather than through empirical observation of differential response ratios between gases.[9,20] Pattern recognition on arrays of differently cation-engineered ferrite composites offers a near-term path to discrimination that does not require fundamental advances in single-sensor sensing chemistry, but this approach has not been implemented for any ferrite composite configuration in the indexed literature.[1,9]

6.2 Humidity Interference

Most chemiresistive sensing studies, including composite ferrite work, are conducted below 40% relative humidity, a condition that does not replicate agricultural environments, mining atmospheres, or clinical exhaled-breath matrices where NH_3 and H_2S monitoring is targeted.[1,2,4] Water vapor competes with analyte molecules at surface oxygen adsorption sites, reducing accessible vacancy density and shifting baseline resistance in ways that fixed-temperature calibration cannot reliably correct.[2,4] For ferrite composites specifically, whether p-n depletion barriers widen or narrow as water vapor displaces adsorbed oxygen at the heterojunction has not been examined for any composite type in the indexed literature.[9,20,45] This is not a minor calibration issue: humidity shifts that alter the baseline depletion state modify both the magnitude and apparent direction of response to a fixed analyte concentration, not only the signal-to-noise ratio.[1,9] Temperature-modulated humidity compensation, discussed in the broader oxide sensor literature, remains experimentally unvalidated for ferrite composite architectures of any type.[1] Type III polymer-ferrite composites carry an additional vulnerability because conducting polymer networks are more permeable to water vapor than oxide-oxide contacts at equivalent temperatures, undermining the practical value of room-temperature operation.[23,44]

6.3 Long-term Stability

The only direct long-term stability observation in the indexed

composite ferrite corpus is the unsatisfactory durability reported for $ZnFe_2O_4$/graphene quantum dot composites during acetone cycling; no other entry in Table 3 addresses the question at all.[9] Extended performance records beyond 7 days of continuous operation are absent for every other composite ferrite architecture in this review, which means published response values and detection limits are single-session measurements without a validated durability basis.[9,44] For Cu-substituted composite systems, the CuS reversibility question is separately unresolved. Cu^{2+} can react with H_2S to form conductive CuS, adding a chemical transformation response pathway alongside ionosorption, but whether CuS reconverts during recovery and whether composite architecture modifies this conversion kinetics has not been tested in any indexed study.[9,44] Distinguishing drift from heterojunction barrier degradation versus ferrite phase structural change as the primary failure mechanism requires operando characterisation techniques not yet applied to any ferrite composite gas sensor.[13,14]

6.4 Operating Temperature and Architecture Conflict

Type I and Type II composite entries in Table 3 produced their strongest response values at 250–290°C.[9,53] Type III polymer-ferrite composites operate at room temperature but lose structural integrity above approximately 150°C, making the two architecture classes mutually exclusive across a temperature range that represents a substantial gap in the design space.[23,44] Room-temperature operation without a polymer phase is achievable within Type II, as the $ZnFe_2O_4$/graphene quantum dot and $rGO/WO_3/ZnFe_2O_4$ entries demonstrate, but the reported instability of the quantum dot system shows that room-temperature Type II performance currently trades durability for reduced thermal requirement.[9] MXene-ferrite composites are the most frequently cited candidate for bridging this gap, with a preliminary room-temperature response documented in recent studies, but the sensing mechanism at the ferrite-MXene contact is uncharacterised and operating condition control is insufficient to permit direct comparison with Type I benchmarks.[15,46]

6.5 Future Priorities-Four experimental targets follow from the gaps documented in Sections 4 and 5, ordered by clarity of the mechanistic basis supporting each.

Zn/Ni co-doped ferrite composites are the highest-priority target because the mechanistic logic is additive and independently grounded in established ferrite physics. Zn^{2+} at A sites redistributes Fe toward B sites, raising hopping carrier density, while Ni^{2+} at B sites introduces a second redox-active cation environment through the Ni^{2+}/Ni^{3+} couple.[9,14] No composite study combines Mössbauer-confirmed site occupancy, systematic Zn:Ni ratio variation, and humidity-controlled sensing data within a single experimental design.[9,12,14] This pairing is simultaneously the most mechanistically motivated and the most experimentally accessible gap in the composite cation engineering literature.

Cu-substituted ferrite composites require long-term H_2S cycling data before they can be specified for monitoring applications. Whether CuS formation during repeated exposure is reversible in composite systems, and whether composite architecture modifies that reversibility, is the single unanswered experimental question that limits translation from laboratory response values to deployment.[9,44]

Rare-earth-doped ferrite composites need direct structural characterisation at the ferrite-second phase contact zone. RE segregation is expected at precisely the boundaries that govern composite sensing performance, yet no indexed study has applied interface-sensitive techniques to this region in a gas sensing context.[13,14,45]

Systematic comparison of Type I through IV architectures for a single controlled ferrite composition does not exist, which means cation engineering effects and architecture effects remain entangled across the entire dataset reviewed here.[9,40] DFT calculations connecting ferrite cation site occupancy to adsorption energetics have been initiated for single-phase $ZnFe_2O_4$,[12] and extending this framework to composite contact geometries would provide the predictive interface design basis that empirical optimisation alone cannot supply.[12,14]

7.0 Conclusions

Cation engineering of the ferrite phase controls carrier density, oxygen vacancy generation, and surface electronic structure, and in nanocomposites those properties propagate to the ferrite-second phase junction to govern depletion layer behaviour and analyte response. $ZnO/ZnFe_2O_4$ composites are the clearest documented case, with interfacial response gains over each isolated phase confirming the oxide-oxide junction as the active performance element. Ni substitution produced the most barrier-sensitive junction behaviour across the dopant classes reviewed. Co-substitution contributed microstructural stability at elevated operating temperatures rather than uniquely advantaged sensing chemistry. Cu substitution altered composite morphology and carrier transport in partner-phase-dependent ways, and the H_2S chemical transformation mechanism attributed to Cu sites remains unconfirmed in any composite cycling study. Type I composites produced the highest absolute response values at elevated temperatures. Type II carbon composites achieved the lowest detection limits alongside partial room-temperature operation, though long-term stability was flagged as unsatisfactory in the only indexed study that examined it. Type III polymer composites enabled room-temperature sensing but cannot sustain structural integrity above 150°C. Type IV bi-ferrite composites produced no gas-sensing data in any indexed study.

Selectivity between reducing gases remains unresolved across all four composite types. Humidity-resolved performance data and stability records extending beyond one week are absent from the indexed literature for every analyte and composite architecture reviewed, which means published detection limits and response values describe dry, short-duration conditions only. Cation site occupancy and composite junction type are independently documented as performance variables throughout this review. Their combination within a single dopant-resolved composite experiment has not been demonstrated for any of the five dopant classes covered here. Zn/Ni co-doped ferrite composites with Mössbauer-confirmed site occupancy, systematic ratio variation, and humidity-controlled sensing conditions represent the clearest first experimental target, connecting the ferrite phase physics of Section 4 to the composite junction framework of Sections 5 and 6 through a study design no indexed work has yet implemented.

References

[1] Bulemo P, Kim D, Shin H, Cho H-J, Koo W, Choi S-J, Park C, Ahn J, Güntner A, Penner RM, Kim I. Selectivity in Chemiresistive Gas Sensors: Strategies and Challenges. Chem Rev. 2025;125:4111-83.

[2] Li H-Y, Lee C-S, Kim DH, Lee J. Flexible Room-Temperature NH_3 Sensor for Ultrasensitive, Selective, and Humidity-Independent Gas Detection. ACS Appl Mater Interfaces. 2018;10(33):27858-67.

[3] Shaik R, Kampara RK, Kumar A, Sharma C, Kumar M. Metal oxide nanofibers based chemiresistive H_2S gas sensors. Coord Chem Rev. 2022;464:214752.

[4] Xuan J, Zhao G, Sun M, Jia F, Wang X, Zhou T, Yin G, Liu B. Low-temperature operating ZnO-based NO_2 sensors: a review. RSC Adv. 2020;10:39786-807.

[5] Nikolić MV, Milovanović VM, Vasiljevic Z, Stamenkovic Z. Semiconductor Gas Sensors: Materials, Technology, Design, and Application. Sensors. 2020;20(22):6694.

[6] Chen Y, Cao Y. Ultrasensitive and low detection limit of acetone gas sensor based on ZnO/SnO_2 thick films. RSC Adv. 2020;10:35958-65.

[7] Vishnuraj R, Karuppanan KK, Aleem M, Pullithadathil B. Boosting the performance of NO_2 gas sensors based on n-n type mesoporous $ZnO@In_2O_3$ heterojunction nanowires: in situ conducting probe atomic force microscopic elucidation of room temperature local electron transport. Nanoscale Adv. 2020;2:4785-97.

[8] Sun K, Zhan G, Chen H-C, Lin S. Low-Operating-Temperature NO_2 Sensor Based on a CeO_2/ZnO Heterojunction. Sensors. 2021;21(24):8269.

[9] Zhang R, Qin C, Bala H, Wang Y, Cao J. Recent Progress in Spinel Ferrite (MFe_2O_4) Chemiresistive Based Gas Sensors. Nanomaterials. 2023;13(15):2188.

[10] Chen H, Chen H, Chen J, Song M. Gas Sensors Based on Semiconductor Metal Oxides Fabricated by Electrospinning: A Review. Sensors. 2024;24(10):2962.

[11] Gai L-Y, Lai R, Dong X, Wu X, Luan Q-T, Wang J, Lin H, Ding W, Wu G-L, Xie W. Recent advances in ethanol gas sensors based on metal oxide semiconductor heterojunctions. Rare Met. 2022;41:1818-42.

[12] Li J, Cheepurupalli KK, English NJ, Bandaru S, Zhang X. Unraveling cation distribution and defect roles in substituted ferrite performance: An atomistic DFT study. J Appl Phys. 2025. doi:10.1063/5.0287154.
[13] Tatarchuk T. Studying the Defects in Spinel Compounds: Discovery, Formation Mechanisms, Classification, and Influence on Catalytic Properties. Nanomaterials. 2024;14(20):1640.
[14] Mataev MM, Madiyarova AM, Abdraimova M, Tursyn Z, Ramachandran K. Structure Property-Application Relationships of Spinel Ferrite Nanoparticles: From Synthesis to Functional Systems. Int J Mol Sci. 2026;27(5):2096.
[15] Nath VG, Ray S, Rodney J, Bharath SP, Roy S, Tarafder K, Subramanian A, Kim BC. Mechanistic insight and first principle analysis of cation-inverted zinc ferrite nanostructure: A paradigm for ppb-level room temperature NO sensor. Chem Eng J. 2024. doi:10.1016/j.cej.2024.151873.
[16] Kotresh S, Ravikiran Y, Vijayakumari S, Thomas S. Interfacial p-n heterojunction of polyaniline-nickel ferrite nanocomposite as room temperature liquefied petroleum gas sensor. Compos Interfaces. 2017;24:549-61.
[17] Liang J, Zou Z, Zhao Z, Hui B, Tian W, Zhang K. Intelligent Gas Detection: g-C_3N_4/Polypyrrole Decorated Alginate Paper as Smart Selective NH_3/NO_2 Sensors at Room Temperature. Inorg Chem. 2024. doi:10.1021/acs.inorgchem.4c01242.
[18] Huo Y, Qiu L, Wang T, Yu H, Yang W, Dong X, Yang Y. P-N Heterojunction formation: Metal Sulfide@Metal Oxide Chemiresistor for ppb H_2S Detection from Exhaled Breath and Food Spoilage at Room Temperature. ACS Sens. 2024. doi:10.1021/acssensors.4c00866.
[19] Mkwae PS, Kortidis I, Kroon RE, Leshabane N, Jozela M, Swart H, Nkosi S. Insightful acetone gas sensing behaviour of Ce substituted $MgFe_2O_4$ spinel nano-ferrites. J Mater Res Technol. 2020;9:16252-69.
[20] Yang S, Lei G, Xu H, Lan Z, Wang Z, Gu H. Metal Oxide Based Heterojunctions for Gas Sensors: A Review. Nanomaterials. 2021;11(4):1026.
[21] Norizan MN, Abdullah N, Halim NA, Demon S, Mohamad IS. Heterojunctions of rGO/Metal Oxide Nanocomposites as Promising Gas-Sensing Materials: A Review. Nanomaterials. 2022;12(13):2278.
[22] Yan Y, Yang G, Xu J, Zhang M, Kuo C, Wang S. Conducting polymer-inorganic nanocomposite-based gas sensors: a review. Sci Technol Adv Mater. 2020;21:768-86.
[23] Alharthy RD, Saleh ASM. A Novel Trace-Level Ammonia Gas Sensing Based on Flexible PAni-$CoFe_2O_4$ Nanocomposite Film at Room Temperature. Polymers. 2021;13(18):3077.
[24] Ramasamy T, Satheesh LG, Selvaraj V, Bazaka O, Levchenko I, Bazaka K, Mandhakini M. Spinel $CoFe_2O_4$ Nanoflakes: A Path to Enhance Energy Generation and Environmental Remediation Potential of Waste-Derived rGO. Nanomaterials. 2022;12(21):3822.
[25] Sanchez-Lievanos KR, Stair JL, Knowles KE. Cation Distribution in Spinel Ferrite Nanocrystals: Characterization, Impact on their Physical Properties, and Opportunities for Synthetic Control. Inorg Chem. 2021. doi:10.1021/acs.inorgchem.1c00040.
[26] Andersen HL, Saura-Múzquiz M, Granados-Miralles C, Canévet E, Lock N, Christensen M. Crystalline and magnetic structure-property relationship in spinel ferrite nanoparticles. Nanoscale. 2018;10(31):14902-14.
[27] Soudani I, Brahim KB, Oueslati A, Slimi H, Aydi A, Khirouni K. Investigation of structural, morphological, and transport properties of a multifunctional Li-ferrite compound. RSC Adv. 2022;12:18697-708.
[28] Dojčinović MP, Vasiljevic Z, Pavlović V, Barišić D, Pajić D, Tadic N, Nikolić MV. Mixed Mg-Co spinel ferrites: Structure, morphology, magnetic and photocatalytic properties. J Alloys Compd. 2021;855:157429.
[29] Ong VH, Pham T, Tien VM, Dinh N, Lan NT, Van Quy N, Bach TN, Lam V, Tung LM, Le AT. Toward a Comprehensive Understanding of Effect of Cation Distribution and M^{2+} Constituent in Spinel Ferrite Nanocrystals MFe_2O_4 (M = Co, Mn, and Ni) on the Electrochemical Response in Sensitive Detection of Chloramphenicol. J Alloys Compd. 2023. doi:10.1016/j.jallcom.2023.169880.
[30] Javed M, Khan A, Kazmi J, Mohamed MA, Khan MN, Hussain M, Bilkees R. Dielectric relaxation and small polaron hopping transport in sol-gel-derived $NiCr_2O_4$ spinel chromite. Mater Res Bull. 2021;138:111242.
[31] Iqbal Y, Shah WH, Khan B, Javed M, Ullah H, Khan N, Khan AR, Asghar G, Safeen A. Small polaron hopping transport mechanism, dielectric relaxation and electrical conduction in $NiAl_2O_4$ electro-ceramic spinel oxide. Phys Scr. 2023;98. doi:10.1088/1402-4896/acd5ba.
[32] Bhargava A, Eppstein R, Sun J, Smeaton MA, Paik H, Kourkoutis L, Schlom D, Toroker MC, Robinson RD. Breakdown of the Small-Polaron Hopping Model in Higher-Order Spinels. Adv Mater. 2020;32. doi:10.1002/adma.202004490.
[33] Sopiha KV, Malyi OI, Persson C, Wu P. Chemistry of Oxygen Ionosorption on SnO_2 Surfaces. ACS Appl Mater Interfaces. 2021;13:33664-76.
[34] Mirabella D, Aldao CM. Dependence of n-Type Metal-Oxide Gas Sensor Response on the Pressure of Oxygen and Reducing Gases. ACS Sens. 2024. doi:10.1021/acssensors.3c02674.
[35] Ciftyürek E, Li Z, Schierbaum K. Adsorbed Oxygen Ions and Oxygen Vacancies: Their Concentration and Distribution in Metal Oxide Chemical Sensors and Influencing Role in Sensitivity and Sensing Mechanisms. Sensors. 2023;23(1):29.
[36] Jung G, Ju S, Choi K, Kim J, Hong S, Park J, Shin W, Jeong Y, Han S, Choi W, Lee J-H. Reconfigurable Manipulation of Oxygen Content on Metal Oxide Surfaces and Applications to Gas Sensing. ACS Nano. 2023. doi:10.1021/acsnano.3c03034.
[37] Ahmad SI. A review on synthesis and magnetic hyperthermia application of spinel nano ferrite. J Umm Al-Qura Univ Appl Sci. 2025. doi:10.1007/s43994-025-00262-1.
[38] Duarte F, Melo A, Oliveira L, Duarte JLS, Oliveira RMPB. Green Synthesis for Antibiotic Photodegradation: Recent Advances and Future Trends. Water. 2025;18(1):39.
[39] Sagayaraj R, Sagayaraj R, Aravazhi S, Chandrasekaran G. Review on structural and magnetic properties of (Co-Zn) ferrite nanoparticles. Int Nano Lett. 2021;11:307-19.
[40] Krishna KG, Parne S, Pothukanuri N, Kathirvelu V, Gandi S, Joshi DC. Nanostructured metal oxide semiconductor-based gas sensors: A comprehensive review. Sens Actuators A Phys. 2022. doi:10.1016/j.sna.2022.113578.
[41] N [first author surname incomplete in source record], Kumar S, Kang HK, Lim W, Lee S, Chae KH, Singh JP. Study of Ferrites Using X-Ray Photoelectron Spectroscopy. ChemistrySelect. 2026. doi:10.1002/slct.202505997.
[42] Wu K, Li J, Zhang C. Zinc ferrite based gas sensors: A review. Ceram Int. 2019. doi:10.1016/j.ceramint.2019.03.086.
[43] Mapossa AB, Mhike W, Adalima JL, Tichapondwa S. Removal of Organic Dyes from Water and Wastewater Using Magnetic Ferrite-Based Titanium Oxide and Zinc Oxide Nanocomposites: A Review. Catalysts. 2021;11(12):1543.
[44] Ranga R, Kumar A, Kumari P, Singh P, Madaan V, Kumar K. Ferrite application as an electrochemical sensor: A review. Mater Charact. 2021. doi:10.1016/j.matchar.2021.111269.
[45] Uma S, Shobana MK. Band structure and mechanism of semiconductor metal oxide heterojunction gas sensor. Inorg Chem Commun. 2023. doi:10.1016/j.inoche.2023.111941.
[46] Imash A, Smagulova G, Kaidar B, Keneshbekova A, Kazhdanbekov R, Velasco L, Mansurov Z. Chemoresistive Gas Sensors Based on Electrospun 1D Nanostructures: Synergizing Morphology and Performance Optimization. Sensors. 2024;24(21):6797.
[47] Maksoud MIAA, Fahim RA, Shalan A, Elkodous AM, Olojede SO, Osman A, Farrell C, Al-Muhtaseb A, Awed AS, Ashour A, Rooney DW. Advanced materials and technologies for supercapacitors used in energy conversion and storage: a review. Environ Chem Lett. 2020;19:375-439.
[48] Nasri A, Pétrissans M, Fierro V, Celzard A. Gas sensing based on organic composite materials: Review of sensor types, progresses and challenges. Mater Sci Semicond Process. 2021;128:105744.
[49] Mu Y, Liang H, Zhang L, Wu H. Ferrite-based composites and morphology-controlled absorbers. Rare Met. 2022;41:2943-70.

[50] Jasim N, Ebrahim S, Ammar SH. A comprehensive review on photocatalytic degradation of organic pollutants and microbial inactivation using Ag/$AgVO_3$ with metal ferrites based on magnetic nanocomposites. Cogent Eng. 2023. doi:10.1080/23311916.2023.2228069.
[51] Zeng H, Liang K, Jiang L, Zhao D, Kong B. Electrochemical Sensing Mechanisms and Interfacial Design Strategies of Mesoporous Nanochannel Membranes in Biosensing Applications. Acc Chem Res. 2025. doi:10.1021/acs.accounts.4c00764.
[52] Alaghmandfard A, Ghandi K. A Comprehensive Review of Graphitic Carbon Nitride (g-C_3N_4)-Metal Oxide-Based Nanocomposites: Potential for Photocatalysis and Sensing. Nanomaterials. 2022;12(2):294.
[53] Jian Y, Hu W, Zhao Z, Cheng P, Haick H, Yao M, Wu W. Gas Sensors Based on Chemi-Resistive Hybrid Functional Nanomaterials. Nano-Micro Lett. 2020;12. doi:10.1007/s40820-020-0407-5.
[54] Leve Z, Iwuoha E, Ross N. The Synergistic Properties and Gas Sensing Performance of Functionalized Graphene-Based Sensors. Materials. 2022;15(4):1326.
[55] Li T, Yin W, Gao S, Sun Y, Xu P, Wu S, Kong H, Yang G, Wei G. The Combination of Two-Dimensional Nanomaterials with Metal Oxide Nanoparticles for Gas Sensors: A Review. Nanomaterials. 2022;12(6):982.
[56] Meng F, Xin R, Li S. Metal Oxide Heterostructures for Improving Gas Sensing Properties: A Review. Materials. 2023;16(1):263.
[57] Pathania A, Dhanda N, Verma R, Sun AC, Thakur P, Thakur A. Review — Metal Oxide Chemoresistive Gas Sensing Mechanism, Parameters, and Applications. ECS Sens Plus. 2024;3. doi:10.1149/2754-2726/ad2152.
[58] Tian X, Cui X, Lai T, Ren J, Yang Z, Xiao M, Wang B, Xiao X, Wang Y. Gas sensors based on TiO_2 nanostructured materials for the detection of hazardous gases: A review. Nano Mater Sci. 2021. doi:10.1016/j.nanoms.2021.05.011.
[59] Yang S, Jiang C, Wei S. Gas sensing in 2D materials. Appl Phys Rev. 2017;4:021304.